npj | computational materials

Article

Published in partnership with the Shanghai Institute of Ceramics of the Chinese Academy of Sciences

https://doi.org/10.1038/s41524-026-02212-9

The comparison between the Pt-Rh thermodynamic database from machine learning interatomic potential and first-principles calculations

Check for updates

Arkapol Saengdeejing[1] ✉, Ryoji Sahara[1], Hiori Kino[1,2], Yoshiyuki Kawazoe[3,4], Kazuyuki Higashino[5] & Toyohiro Chikyow[1]

Platinum–rhodium alloys are one of the prominent alloys used in high-temperature and high-corrosion environments. Pt and Rh maintain a single solid-solution phase up to high temperatures. To develop and design a part for use in the field, many techniques, tools, and software in combination, such as the phase-field method for microstructure prediction and the finite element method for stress analysis, are required. These methods require additional data, such as thermodynamic stability. Developing a thermodynamic database is costly and time-consuming. To accelerate the construction of a thermodynamic database, advanced computational methods are usually incorporated into the process to facilitate data acquisition required for thermodynamic assessment. With the advancement of machine learning techniques, many tools for computational materials science have been available at a fraction of the computational resources required when performing similar calculations using traditional techniques. In this study, we employed machine learning interatomic potential (MLIP) to calculate the thermodynamic properties required for the CALPHAD-type thermodynamic assessment of the Pt-Rh binary system. First-principles calculations were performed to compare the thermodynamic database constructed from the MLIP and first-principles calculation data. The phase diagram calculated from MLIP achieved an accuracy similar to that of the phase diagram calculated using more first-principles calculations.

Phase diagram is considered on of the most important tools for materials science community. Traditional phase diagram is typically constructed directly from experiment result. The modern approach of phase diagram construction is mostly based on the CALculation of PHAse Diagram (CALPHAD) methodology[1], which is based on the construction of the thermodynamic databases. Several experimental and theoretical investigations are required to construct thermodynamic databases for alloy research and development. This is a costly and time-consuming process, particularly in terms of experimental procedures. First-principles calculations help reduce the number of experiments required but still require considerable computational resources. With advancements in machine learning techniques, several models of tailor-made or universal interatomic potentials have been proposed[2–5], which can achieve an accuracy similar to that of first-principles calculations with several orders of magnitude fewer computational resources. Using machine learning interatomic potential (MLIP), the construction of a preliminary thermodynamic database entirely without experimental data can help accelerate the thermodynamic database development process.

Only a few alloy systems are suitable for high-temperature and high-corrosion environments. Platinum–rhodium (Pt-Rh) alloys are among the most prominent alloys used in these environments. Owing to the nature of Pt and Rh, they maintain a single solid-solution phase across the composition range up to 2000 K[6]. Several experimental and theoretical investigations have been performed on Pt-Rh systems [7–17]. Because most Pt applications involve catalytic reactions, many studies have focused on its surface properties. Very limited thermodynamic data exist for the Pt-Rh systems. The solid-liquid equilibria have been investigated by Müller[18] and Acken[19]. Jacob et al.[11] performed the solid state galvanic cell experiment to determine the activity of the Pt-Rh alloys between 900

[1]National Institute for Materials Science, Tsukuba, Japan. [2]The Institute of Statistical Mathematics, Tokyo, Japan. [3]NICHe Tohoku University, Sendai, Japan. [4]Department of Physics, SRM University-AP, Amaravati, India. [5]NETS Co. Ltd., Tsurugashima, Japan. ✉e-mail: saengdeejing.arkapol@nims.go.jp

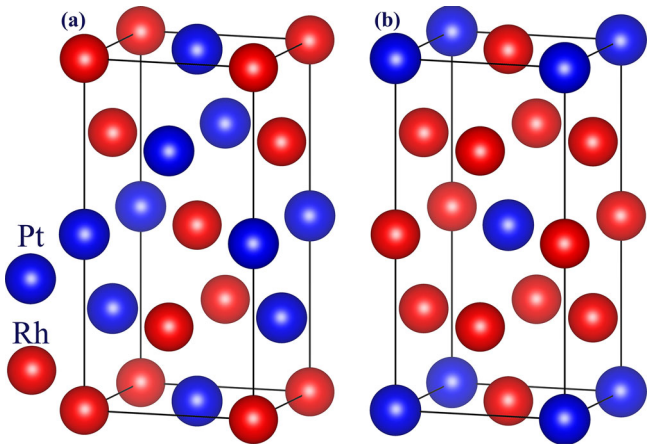


Fig. 1 | Ordered Pt–Rh crystal structures. a Unit cell of the ordered PtRh-I4$_1$/amd phase. **b** Unit cell of the ordered PtRh$_3$-I4/mmm phase. Blue and red atoms represent Pt and Rh, respectively.

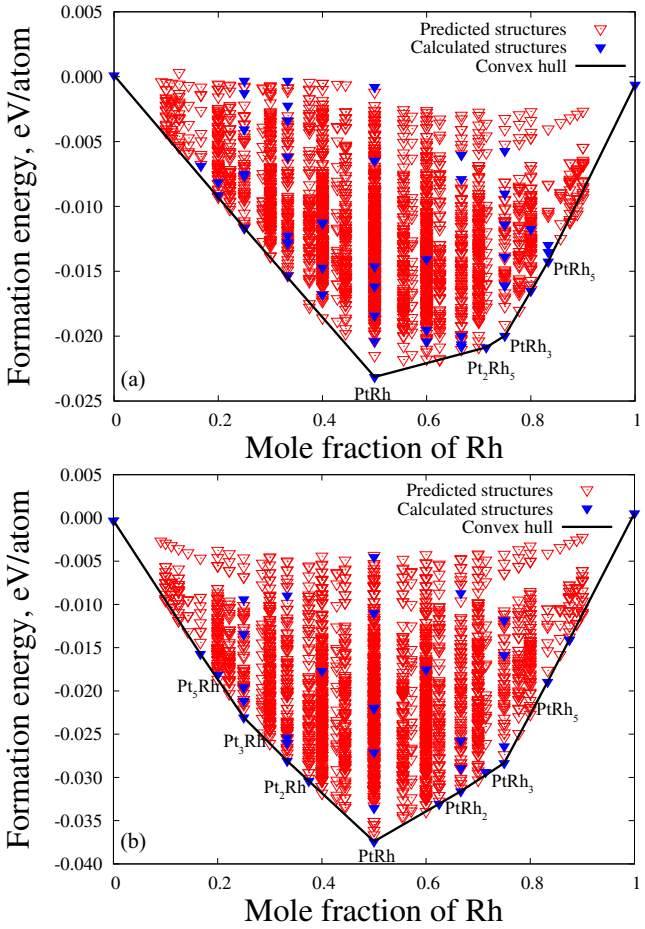


Fig. 2 | Cluster expansion results for the fcc Pt-Rh binary system calculated using DFT and MLIP. a DFT results. **b** MLIP results. The solid line represents the convex hull connecting the lowest-energy structures across the composition range. The solid symbols represent the formation energies of the structures used for the cluster expansion calculations, whereas the open symbols represent the predicted formation energies of the sampled structures obtained from the cluster expansion model.

and 1300 K. The current phase diagram of the Pt-Rh binary system[6] is based on a combination of experiments by Múller and Acker[18,19] and a Monte Carlo simulation by Lu et al.[9,10].

In this work, we attempt to construct the thermodynamic database for the Pt-Rh binary system via the CALPHAD methodology using either the data from MLIP or the first-principles calculations.

Results

Ground state stability calculations

For the Pt-Rh binary system, two intermediate phases (PtRh-I4$_1$/amd and PtRh$_3$-I4/mmm) have been reported in the literature[9,10,14,15,20]. Based on the 0 K thermodynamic stability investigations by Lu et al.[10], Yuge et al.[14], and Curtarolo et al.[20] using cluster expansion method (CEM)[21] on the fcc lattice, both PtRh-I4$_1$/amd and PtRh$_3$-I4/mmm have been reported. Figure 1 shows the unit cell of PtRh-I4$_1$/amd and PtRh$_3$-I4/mmm. Two CEMs were performed using the energies calculated from first-principles calculations based on density functional theory (DFT) and MLIP. The CEM results are shown in Figure 2. The CEM results from DFT were generally similar to those reported by Curtarolo et al. [20]. However, some differences were observed between the DFT and MLIP results. There are four thermodynamically most stable phases (PtRh, Pt$_2$Rh$_5$, PtRh$_3$, and PtRh$_5$) along the convex hull in the DFT results, whereas there are additional stable phases (Pt$_5$Rh, Pt$_3$Rh, Pt$_2$Rh, and PtRh$_2$) present in the MLIP that do not appear in the DFT results. In the DFT calculations, most of the additional structures were positioned slightly above the convex hull. Only Pt$_3$Rh, which is the anti-site structure of PtRh$_3$-I4/mmm, was shown to be significantly more stable than the DFT results. In the literature[20] and DFT results, Pt$_3$Rh-I4/mmm is a metastable phase, where the stability is slightly above the convex hull.

Although there are some differences between the DFT and MLIP results, the PtRh-I4$_1$/amd and PtRh$_3$-I4/mmm phases are the commonly observed in both calculation results. Thus, PtRh-I4$_1$/amd and PtRh$_3$-I4/mmm will be considered for this study. In addition to previously mentioned phases, the Pt$_3$Rh-I4/mmm structure, which is the anti-site of the PtRh$_3$-I4/mmm, was also considered. Table 1 lists information related to some stable and metastable fcc-ordered structures from the CEM results. Figure 3 shows the calculated formation enthalpies, according to the Equation (16), of Pt$_3$Rh, PtRh, PtRh$_3$, and some higher-order structures (R$\bar{3}$ m and P4/mmm) from the DFT and MLIP calculations. The high-symmetry ordered structures are less stable than those of the results predicted from the CEM. In addition, all the enthalpies of formation calculated from the MLIP seems to be more negative than the DFT results. It seem to be systematically different between MLIP and DFT. From Figure 2, it can be seen that all the energies calculated from MLIP are systematically lower than DFT results. The differences between MLIP and DFT values are somewhere between 0.7 and 1.5 kJ/mol-atom. Typically, the experimental uncertainties from the measurement can sometime varies from ± 5% to ± 50% owing to the different techniques and sample preparations[22]. The differences between MLIP and DFT fall on the higher end comparing to the experiment. However, the convex hull shapes were similar between the two results. Compared with other alloy systems such as Al-Ni[23] and Cu-Hf[24] binary, the enthalpy of formation for all the structures in the Pt-Rh system is considered small, comparing to the Al-Ni system, which is between −60 to −40 kJ/mol-atom, or between −18 to −7 kJ/mol-atom in the Cu-Hf system. This implies that these structures are unstable at elevated temperatures.

Solid solubility phase calculations

To incorporate the solid solubility of the ordered compounds, two-sublattice models, which can represent the continuous changing of the concentration of element in each sublattice, were adopted for all three structures ((Pt,Rh)$_3$(Pt,Rh) and (Pt,Rh)(Pt,Rh)). By introducing two-sublattice model[25] based on the compound energy formalism (CEF)[26], the configurational entropy from the mixing between different elements in each sublattice can be considered as the long range ordering contribution to the phase. For the Pt$_3$Rh and PtRh$_3$ phases, only single two-sublattice model is required to represent both compounds. The 0 K and the finite-temperature energies were calculated for all end-members related to all three phases. Since the stability of all ordered compounds in the Pt-Rh system are

Table 1 | Crystal symmetry and lattice parameters of all compounds investigated in this work

Phases	Pearson	SG	# atom	Lattice parameter						Ref.
				a	b	c	α	β	γ	
Pt_3Rh-P4/mmm	cP4	$Pm\bar{3}$ m	4	3.9340(3.9318)	3.9340(3.9318)	3.9340(3.9318)	90(90)	90(90)	90(90)	52
Pt_3Rh-I4/mmm	tI8	I4/mmm	8	3.9367(3.9331)	3.9367(3.9331)	7.8606(7.8587)	90(90)	90(90)	90(90)	This work (CEM)
PtRh-$m\bar{3}$ m	tP4	P4/mmm	4	2.7119(2.7559)	2.7119(2.7559)	3.3423(3.8926)	90(90)	90(90)	90(90)	This work (CEM)
PtRh-$R\bar{3}m$	N/A	$R\bar{3}$ m	6	2.7697(2.7620)	2.7697(2.7620)	13.4075(13.4421)	90(90)	90(90)	120(120)	52
PtRh-$I4_1$/amd	tI8	$I4_1$/amd	8	3.8994(3.8919)	3.8994(3.8919)	7.8111(7.8051)	90(90)	90(90)	90(90)	9
$PtRh_3$-P4/mmm	tI8	$Pm\bar{3}$ m	8	3.8672(3.8591)	3.8672(3.8591)	3.8672(3.8591)	90(90)	90(90)	90(90)	This work (CEM)
$PtRh_3$-I4/mmm	cP4	I4/mmm	4	3.8673(3.8569)	3.8673(3.8569)	7.7377(7.7260)	90(90)	90(90)	90(90)	52

The values in parentheses are from DFT calculations

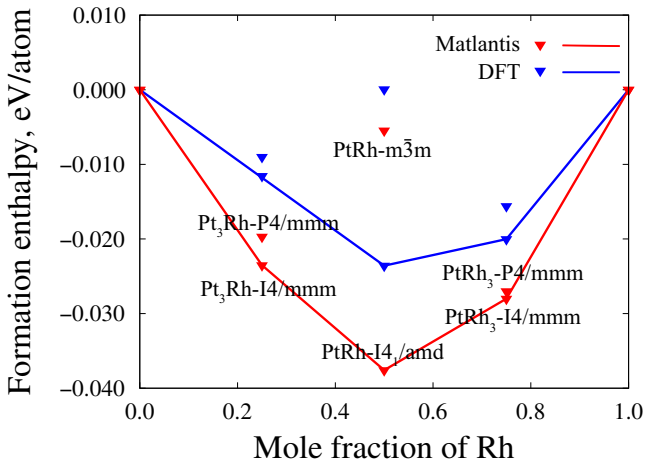


Fig. 3 | Comparison of the calculated 0 K enthalpies of formation of Pt3Rh, PtRh, and PtRh3 obtained using MLIP and DFT. Blue and red symbols represent the MLIP and DFT results, respectively. The solid line represent the convex hull connecting the lowest-energy structures across the composition range. the symbols indicate the formation energies of the individual structures. The symbols are the formation energy of each structure.

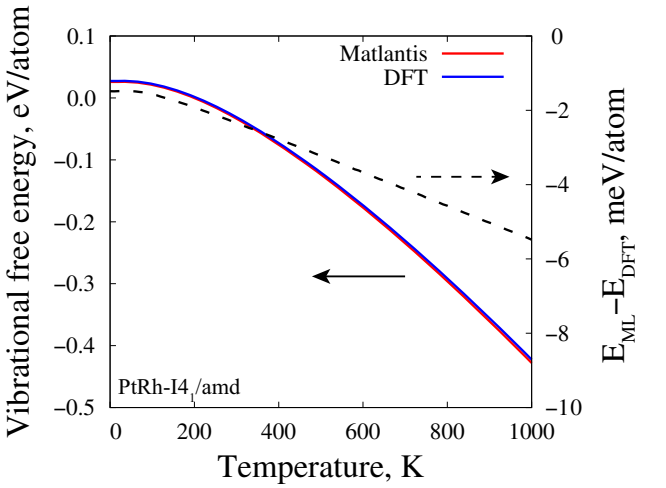


Fig. 4 | Calculated vibrational free energy of the PtRh-$I4_1$/amd phase obtained using MLIP and DFT as a function of temperature. Red and blue curves represent the MLIP and DFT results, respectively. The dashed line shows the energy difference between the MLIP and DFT results.

presented at the low temperature, only the harmonic-vibrational contribution is considered. The anharmonic-vibrational contribution, which typically important where the stability of the structure is extended to a very high temperature, is not considered. Figure 4 shows the calculated finite-temperature vibrational free energy of PtRh-$I4_1$/amd using MLIP and DFT. The differences between the MLIP and DFT results are very small at low temperatures but increase with temperature. At 1000 K, the differences are approximately 5.5 meV/atom (~ 550 J/mol-atom). Since PtRh-$I4_1$/amd is only stable below 300 K. The vibrational contribution should be comparable from both MLIP and DFT calculations. Figure 5 shows the calculated Gibbs free energy for the formation of PtRh-$I4_1$/amd. The calculated Gibbs free energy of formation of PtRh-$I4_1$/amd is positive for both MLIP and DFT. This indicates that PtRh-$I4_1$/amd phase is thermodynamically unstable above room temperature. The result follows a linear relationship according to the Neumann–Kopp approximation in Equation (11). The slopes of the DFT and MLIP were slightly different. The formation entropy was estimated from the negative slope of the plot. The formation entropy dictates the stability of the structure in relation with their reference phases. The positive entropy of formation leads to the higher stability of the structure (the Gibbs free energy become more negative), conversely for the negative entropy of formation. The enthalpy and entropy of formation required for thermodynamic modeling were derived and are listed in Table 2. The entropy of formation for all of the structures is negative. It indicates the decrease in the structural stability as the temperature increases.

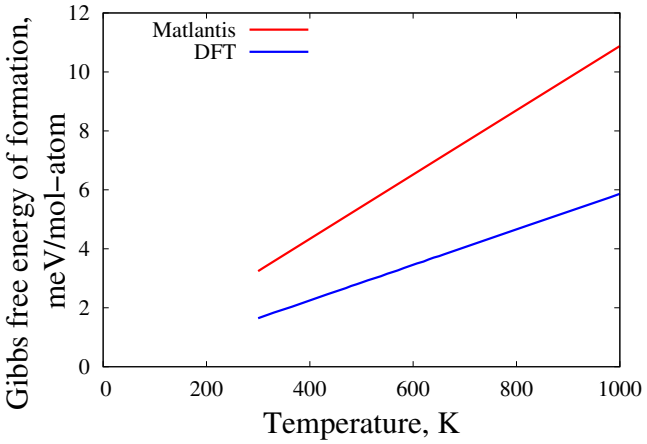


Fig. 5 | Calculated Gibbs free energy of formation of the PtRh-$I4_1$/amd phase obtained from MLIP and DFT. The red and blue curves represent the MLIP and DFT results, respectively.

Mixing interaction calculations

To evaluate the interaction parameters for both sublattice models, six different SQSs are constructed to represent the random mixing of the Pt and Rh elements in each sublattice. Figure 6 shows the 64-atom unit cell of the

Table 2 | Calculated enthalpies of formation ($\Delta_F H$), entropies of formation ($\Delta_F S$), and k-point meshes for all intermediate compounds and end-members obtained from MLIP

Structures	Compositions	Formation energy		Γ
		$\Delta_F H$, eV/atom	$\Delta_F S$, × 10^{-6} eV/atom-K	k-point mesh
Pt_3Rh-P4/mmm	Pt_3Rh	−0.0197(−0.0090)	−5.7999(−3.9969)	13 × 13 x 13
Pt_3Rh-I4/mmm	Pt_3Rh	−0.0235(−0.0200)	−6.6686/−6.6228 (−4.3144/−3.6410)	15 × 15 x 7
PtRh-R$\bar{3}$ m	PtRh	−0.0055(0.0001)	−6.7451(−1.8621)	17 × 17 x 5
PtRh-$I4_1$/amd	PtRh	−0.0376(−0.0236)	−10.9029/−10.8742 (−6.0105/−5.9512)	13 × 13 x 7
$PtRh_3$-P4/mmm	$PtRh_3$	−0.0270(−0.0156)	−5.6501(−6.1509)	13 × 13 x 13
$PtRh_3$-I4/mmm	$PtRh_3$	−0.0280(−0.0200)	−6.6463/−6.6524 (−6.1059/−6.1377)	15 × 15 x 7

The values in parentheses are from DFT calculations. The underline numbers are the entropy of formation calculated from CALPHAD.

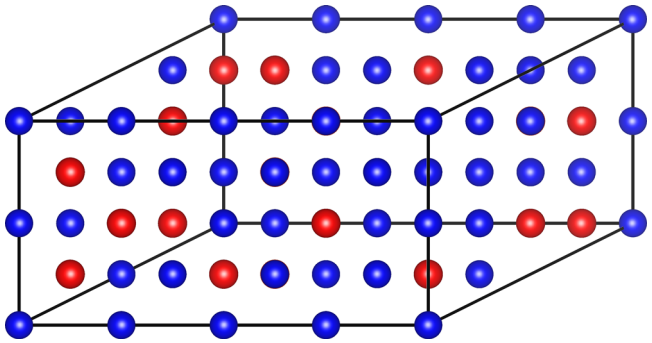


Fig. 6 | Illustration of PtRh-$I4_1$/amd SQS unit cell. Blue and red atoms represent Pt and Rh, respectively.

Pt(Pt,Rh)-$I4_1$/amd SQS. The calculated correlation functions of the pair- and triplet-cluster show that from the smallest to the 15th pair-cluster are matched with the theoretical correlation function of random configuration. The triplet-cluster correlation functions are also matched from smallest up to the 17th cluster. Table 3 lists the calculated Pt(Pt,Rh)-$I4_1$/amd correlation functions for different types and sizes of clusters compared with the theoretical random values. Table 4 lists all the SQSs generated for this study. Owing to limited computational resources, the finite-temperature thermodynamic properties were not evaluated using DFT. Only the 0 K energies of the SQSs were calculated. However, both the 0 K and finite-temperature free energies of all SQSs were calculated using MLIP. The results listed in Table 5 were used to evaluate the interaction parameters of the thermodynamic model. Regular solution models (only the temperature-independent 0th-order interaction parameters) were considered for both PtRh-$I4_1$/amd and $PtRh_3$-I4/mmm. The evaluated interaction parameters are listed in Table 6.

For disordered phases, Table 4 lists the SQSs used for the calculations of mixing energy. Figure 7 shows the mixing enthalpy of the fcc and hcp disordered states at different Rh concentrations calculated using DFT. The mixing enthalpies of the fcc-disordered samples were not symmetrical, whereas those of the hcp-disordered samples were small and remained mostly positive. The inset shows a comparison of the bcc-disordered results. The bcc-disordered enthalpies of mixing were significantly more stable than the fcc- and hcp-disordered enthalpies. This characteristic is commonly observed in the system that sizable displacements occurred[27]. For the bcc lattice that contained a moderately difference in the atomic size between the two elements, it is likely that this situation might appear. The SQS tended to collapse into a more stable ordered structure. An example and verification of similar behavior were explained and discussed in our previous publication[28]. Thus, these bcc-disordered results were excluded from the evaluation. The hcp-disordered enthalpies of mixing were relatively small. Thus, the hcp-disordered model was treated as an ideal solution model (the interaction

Table 3 | Calculated pair and triplet correlation functions of Pt($Pt_{0.5}Rh_{0.5}$)-$I4_1$/amd SQS compared with those of the corresponding perfectly random configuration

Cluster type	Cluster size,	Correlation function	
	Å	Calculated	Random
Pair	2.7558	0.0000	0.0000
	3.8919	0.0000	0.0000
	4.7688	0.0000	0.0000
	4.7753	0.0000	0.0000
	5.5040	0.0000	0.0000
	6.1554	0.0000	0.0000
	6.1688	0.0000	0.0000
	7.2826	0.0000	0.0000
	7.2868	0.0000	0.0000
	7.2939	0.0000	0.0000
	7.7839	0.0000	0.0000
	7.8051	0.0000	0.0000
	8.2573	0.0000	0.0000
	8.2673	0.0000	0.0000
	8.7026	0.0000	0.0000
	8.7216	-0.5000	0.0000
Triplet	3.8919	0.0000	0.0000
	4.7688	0.0000	0.0000
	4.7688	0.0000	0.0000
	4.7753	0.0000	0.0000
	4.7753	0.0000	0.0000
	4.7753	0.0000	0.0000
	4.7753	0.0000	0.0000
	4.7753	0.0000	0.0000
	5.5040	0.0000	0.0000
	5.5040	0.0000	0.0000
	5.5040	0.0000	0.0000
	6.1554	0.0000	0.0000
	6.1554	0.0000	0.0000
	6.1554	0.0000	0.0000
	6.1688	0.0000	0.0000
	6.1688	0.0000	0.0000
	6.1688	0.0000	0.0000

parameters were equal to zero). The symbols in Fig. 8 show the calculated 0 K fcc-disordered mixing energy compared with both DFT and MLIP. The 0 K mixing energy of fcc-disordered calculated from the MLIP appeared symmetrical, which slightly differed from the DFT results, where the 0 K mixing enthalpy was slightly asymmetric. There are some differences between the mixing energies calculated using MLIP and DFT. At equiatomic concentrations, the MLIP value is approximately 700 J/mol-atom lower than the DFT value. The solid and dashed lines represent the mixing energies calculated from the CALPHAD model fitted to the MLIP and DFT data, respectively. There were some differences between the MLIP and DFT results; however, as the temperature increased, the mixing energy behavior became similar to that of DFT. The difference in the temperature-dependent terms of the interaction parameters was approximately 3 J/mol-atom-K. The extracted disordered interaction parameters are listed in Table 6. Both the MLIP and the DFT temperature-dependent parameters are positive. This indicates that the fcc-disordered excess energy term become smaller as increasing temperature. However, the fcc-disordered phase is most stabilized owing to the larger negative contribution from the ideal mixing term (Eq. (7)). In the case of the MLIP phase diagram, the fcc-disordered ideal mixing energy is almost double in value of the excess energy at 500 K and 50 at%Rh. Owing to the lack of data on the liquid phase, only an ideal mixing was considered.

Table 4 | Mixing sites, compositions, and size of all SQSs investigated in this work

Structures	Mixing site	SQS composition	No. atoms	Ref.
fcc	$(A_{0.875},B_{0.125})$	$A_{56}B_8$	64	23
	$(A_{0.75},B_{0.25})$	$A_{12}B_4$	16	53
	$(A_{0.625},B_{0.375})$	$A_{40}B_{24}$	64	23
	$(A_{0.5},B_{0.5})$	A_8B_8	16	53
bcc	$(A_{0.875},B_{0.125})$	$A_{56}B_8$	64	23
	$(A_{0.75},B_{0.25})$	$A_{12}B_4$	16	54
	$(A_{0.625},B_{0.375})$	$A_{40}B_{24}$	64	23
	$(A_{0.5},B_{0.5})$	A_8B_8	16	54
hcp	$(A_{0.875},B_{0.125})$	$A_{56}B_8$	64	23
	$(A_{0.75},B_{0.25})$	$A_{12}B_4$	64	55
	$(A_{0.625},B_{0.375})$	$A_{40}B_{24}$	64	23
	$(A_{0.5},B_{0.5})$	A_8B_8	64	55
PtRh-$I4_1$/amd	(Pt,Rh)Rh	$Pt_{16}Rh_{48}$	64	This work
	Pt(Pt,Rh)	$Pt_{48}Rh_{16}$	64	This work
$PtRh_3$-I4/mmm	$Pt(Pt,Rh)_3$	$Pt_{40}Rh_{24}$	64	This work
	$Rh(Pt,Rh)_3$	$Pt_{24}Rh_{40}$	64	This work
	$(Pt,Rh)Pt_3$	$Pt_{56}Rh_8$	64	This work
	$(Pt,Rh)Rh_3$	$Pt_{56}Rh_8$	64	This work

Phase diagram calculations

Figure 9 shows the calculated phase diagram of the Pt-Rh binary system using only DFT data. Typically, the Gibbs free energy descriptions of CALPHAD are valid up to room temperature (298.15 K). The T^{-1} polynomial term used to describe the Gibbs free energy in CALPHAD results in the Gibbs free energy reaching infinity near 0 K. For the past decade, the CALPHAD community have been developed the 3rd generation model and descriptions for the thermodynamic database by adopting the physical representation to fix the problem for the low-temperature region of the thermodynamic description[29]. However, with the current generation databases, the free energy down to 50 K should be accurate. Table 6 lists all the parameters of the Pt-Rh thermodynamic database. The two ordered phases (PtRh-$I4_1$/amd and $PtRh_3$-I4/mmm) were stable, starting at very low temperatures and destabilizing around −62 °C and −117 °C, respectively. The solubility range for both ordered structures was narrower than that reported in the literature[15]. There are a few possibilities that could contribute to the narrowing of the solubility of the ordered phases. The first is the lack of temperature dependence of the interaction parameters. This can result in narrow solubility ranges for both ordered structures. The other possibility is unaccounted-for short-range ordering. The ordered–disordered transition temperature between PtRh-$I4_1$/amd and fcc-disordered is −63 °C, whereas the result from Monte Carlo simulations from Pohl et al.[15] is −35 °C. The difference is less than 30 °C between the literature and this work. This indicates that the energy descriptions of the ordered and disordered phases are similar to those reported in the literature. All the invariant reactions are listed in Table 7. Figure 10 shows the calculated phase diagram from −200 °C to 100 °C, comparing the results obtained using MLIP and DFT. The solid line is the phase diagram calculated from the MLIP, whereas the dashed line is the phase diagram calculated from the DFT result. The three ordered phases were stable below 0 °C (Pt_3Rh, PtRh, and $PtRh_3$). All three phases exhibited solubility ranges. However, Pt_3Rh exhibits a narrow solubility range (less than 0.03 at% Rh). Comparing to the solubility range from Lu et al.[9], it is clearly seen that our model underestimates the solid-solubility in both PtRh and $PtRh_3$. The exclusion of the short-range ordering contribution might be the reason for the largely underestimation of the solid-solubility range for both phases. Incorporating the order-disorder model[30] might improve the solid-solubility range in both phases. Only one eutectoid reaction, fcc ↔ PtRh + $PtRh_3$ at 69.3 at%Rh and −124 °C, appears in the DFT phase diagram. The order-disorder transition temperature for both PtRh and $PtRh_3$ were -62.6 °C and −117.1 °C, respectively. Two eutectoid reactions appear in the MLIP phase diagram. The first is fcc ↔ Pt_3Rh + PtRh at 25.8 at% Rh and −128 °C. The other is fcc ↔ PtRh + $PtRh_3$ at 65.3 at%Rh and −62 °C. The order-disorder transition temperatures for Pt_3Rh, PtRh, and $PtRh_3$ are −127.46 °C, −15.32 °C, and −38.43 °C, respectively. Table 7 lists all the temperatures and compositions of the invariant reactions in the Pt-Rh binary system. Figure 11 shows the calculated phase diagram, including the liquid phase. The two-phase region between the fcc phase and liquid is very narrow. This indicates the similarity between the Gibbs free energy between liquid and fcc phases. The shapes of the liquidus and solidus were also very close to the ideal solution model. This is because of the very small fcc-disordered interaction parameters. Owing to

Table 5 | Mixing enthalpies calculated from SQSs for the selected interaction parameters of the sublattice models. The values in parentheses are from DFT calculations

Mixing structures	SQS composition	Enthalpy of mixing, meV/atom	Entropy of mixing meV/atom-K
$Pt(Pt_{0.5}Rh_{0.5})$	$Pt_{48}Rh_{16}$	−0.3093(2.3269)	-3.5471×10^{-6}
$Rh(Pt_{0.5}Rh_{0.5})$	$Pt_{16}Rh_{48}$	−3.1216(-3.6378)	-3.0634×10^{-6}
$Pt(Pt_{0.5}Rh_{0.5})_3$	$Pt_{40}Rh_{24}$	−5.9900(−2.4355)	-7.1602×10^{-6}
$Rh(Pt_{0.5}Rh_{0.5})_3$	$Pt_{24}Rh_{40}$	−11.8169(−10.1693)	-5.7584×10^{-6}
$(Pt_{0.5}Rh_{0.5})Pt_3$	$Pt_{56}Rh_8$	1.0571(1.3506)	-1.8027×10^{-6}
$(Pt_{0.5}Rh_{0.5})Rh_3$	Pt_8Rh_{56}	1.1278(-0.8052)	-1.0496×10^{-6}

Table 6 | CALPHAD parameters for the Pt-Rh thermodynamic database

Phases	Parameters	Values	
		MLIP	DFT
fcc	${}^{0}G_{pt}^{fcc}$	${}^{a0}G_{pt}^{fcc}$	
	${}^{0}G_{Rh}^{fcc}$	${}^{a0}G_{Rh}^{fcc}$	
	${}^{0}L_{Pt,Rh}^{fcc}$	$-8725 + 4.53T$	$-5000 + 1.3T$
	${}^{0}L_{Pt,Rh}^{fcc}$	$+1.25T$	$+3000$
bcc	${}^{0}G_{Pt}^{bcc}$	${}^{a0}G_{Pt}^{bcc}$	
	${}^{0}G_{Rh}^{bcc}$	${}^{a0}G_{Rh}^{bcc}$	
hcp	${}^{0}G_{Pt}^{hcp}$	${}^{a0}G_{Pt}^{hcp}$	
	${}^{0}G_{Rh}^{hcp}$	${}^{a0}G_{Rh}^{hcp}$	
Liquid	${}^{0}G_{Pt}^{liq}$	${}^{a0}G_{Pt}^{liq}$	
	${}^{0}G_{Rh}^{liq}$	${}^{a0}G_{Rh}^{liq}$	
	${}^{0}L_{Pt,Rh}^{liq}$	$-8725 + 4.53T$	$-5000 + 1.3T$
	${}^{0}L_{Pt,Rh}^{liq}$	$+1.25T$	$+3000$
PtRh-$I4_1$/amd	${}^{0}G_{Pt_2}^{PtRh}$	$2{}^{a0}G_{pt}^{fcc} + 2000 + 2T$	$2{}^{a0}G_{pt}^{fcc} + 2000 + 2T$
	${}^{0}G_{PtRh}^{PtRh}$	${}^{a0}G_{pt}^{fcc} + {}^{a0}G_{Rh}^{fcc}$ $-7252 + 2.10T$	${}^{a0}G_{pt}^{fcc} + {}^{a0}G_{Rh}^{fcc}$ $-5000 + 1.16T$
	${}^{0}G_{RhPt}^{PtRh}$	${}^{a0}G_{pt}^{fcc} + {}^{a0}G_{Rh}^{fcc}$ $-7252 + 2.10T$	${}^{a0}G_{pt}^{fcc} + {}^{a0}G_{Rh}^{fcc}$ $-5000 + 1.16T$
	${}^{0}G_{Rh_2}^{PtRh}$	$2{}^{a0}G_{Rh}^{fcc} + 2000 + 2T$	$2{}^{a0}G_{Rh}^{fcc} + 2000 + 2T$
	${}^{0}L_{(Pt,Rh):Pt}^{PtRh}$	$-125 + 1.37T$	1000
	${}^{0}L_{(Pt,Rh):Rh}^{PtRh}$	$-1200 + 1.18T$	-1400
$PtRh_3$-$I4/mmm$	${}^{0}G_{Pt_4}^{PtRh_3}$	$4{}^{a0}G_{pt}^{fcc} + 4000 + 4T$	$4{}^{a0}G_{pt}^{fcc} + 4000 + 4T$
	${}^{0}G_{PtRh_3}^{PtRh_3}$	${}^{a0}G_{pt}^{fcc} + 3{}^{a0}G_{Rh}^{fcc}$ $-10807 + 2.57T$	${}^{a0}G_{pt}^{fcc} + 3{}^{a0}G_{Rh}^{fcc}$ $-8000 + 2.38T$
	${}^{0}G_{Rh_3Pt}^{PtRh_3}$	$3{}^{a0}G_{pt}^{fcc} + {}^{a0}G_{Rh}^{fcc}$ $-9075 + 2.57T$	$3{}^{a0}G_{pt}^{fcc} + {}^{a0}G_{Rh}^{fcc}$ $-4500 + 1.55$
	${}^{0}G_{Rh_4}^{PtRh_3}$	$4{}^{a0}G_{Rh}^{fcc} + 4000 + 4T$	$4{}^{a0}G_{Rh}^{fcc} + 4000 + 4T$
	${}^{0}L_{(Pt,Rh):Pt}^{PtRh_3}$	$+400 + 0.70T$	500
	${}^{0}L_{(Pt,Rh):Rh}^{PtRh_3}$	$+435 + 0.41T$	-300
	${}^{0}L_{Pt:(Pt,Rh)}^{PtRh_3}$	$-2300 + 2.76T$	-1000
	${}^{0}L_{Rh:(Pt,Rh)}^{PtRh_3}$	$-4560 + 2.22T$	-4000

[a] SGTE pure elements database[42]

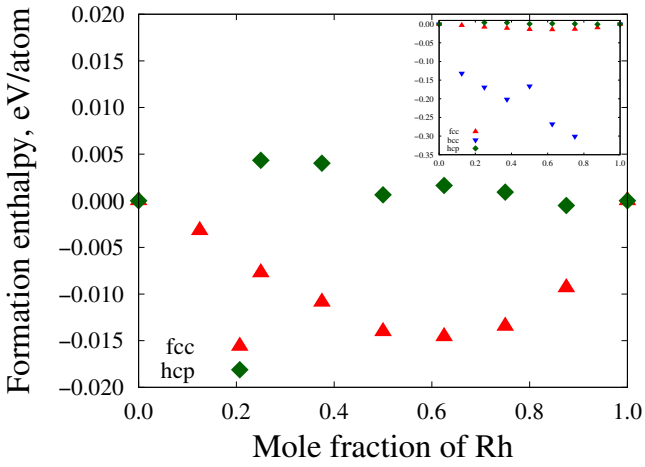


Fig. 7 | Calculated enthalpies of mixing from DFT for fcc and hcp SQS obtained from DFT as a function of composition, with the bcc SQS results shown in the inset for comparision. Upward triangles, downward triangles, and diamonds represent the fcc, bcc, and hcp structures, respectively.

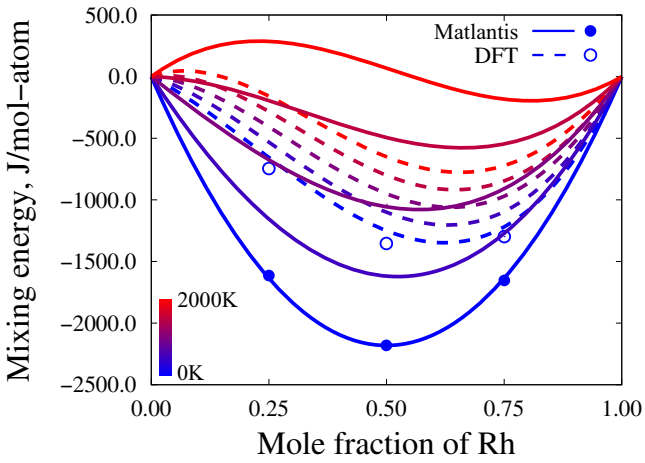


Fig. 8 | Calculated mixing energy of fcc-disordered phase obtained from SQSs using MLIP and DFT. Closed and opened symbols represent the MLIP and DFT results, respectively. Solid and dashed lines represent the mixing energies calculated from the CALPHAD models parameterized using the MLIP and DFT data, respectively. The line color varies from blue (0 K) to red (2000 K), indicating the calculation temperature.

the positive temperature-dependent term in the fcc interaction parameters, it is possible that fcc phase might destabilized or formed a miscibility gap at high temperature. We perform the phase diagram calculation without the liquid phase and found that the fcc-disordered phase transforms to bcc-disordered at the temperature above 4000 K. This temperature is well above the melting temperature of the typical Pt-Rh binary system. This kind of behavior is often observed in many thermodynamic database assessments.

Another system that has the similar characteristic as the Pt-Rh is the Au-Cu system[30]. Both systems contain stable fcc-ordered phases ($L1_0$ and $L1_2$) at low temperature. The stability of fcc-ordered phases in the Au-Cu is higher, reaching around 430 °C for $L1_0$. The liquid–solid phase boundary also differs owing to negative liquid interactions.

Both the MLIP and DFT phase diagrams showed similar results and agreed with those of previously published studies[15]. This proves that, using either MLIP or DFT data, a thermodynamic database can be accurately established. Similar to the implementation of the DFT data in the extended CALPHAD model, MLIP data can be further implemented in the similar manner. In this work, only a simple solid-solution model is implemented. There are more sophisticated models such as the order-disorder model[31], the effective bond energy formalism for a multi-lattice system[32], or the para-equilibrium in multicomponent system[33], which typically need the many data from computationally demanding DFT calculations. With MLIP, the implementation of further complex CALPHAD modeling can be accelerated.

Discussions

In this study, we constructed and compared a thermodynamic database of the Pt-Rh binary system using only data obtained from either MLIP or DFT calculations. The MLIP-calculated thermodynamic properties were comparable to the results of the DFT calculations. The phase diagram calculated using the MLIP results was similar to that calculated using the DFT data. A noticeable difference is the stability of the Pt_3Rh phase in the MLIP phase

diagram, which is not stable in the DFT phase diagram or in previously published literature[10]. However, the DFT results showed that the stability of the Pt_3Rh phase was between the stable and metastable phases on the convex hull. The underestimated solubility range for both PtRh-$I4_1$/amd and $PtRh_3$-I4/mmm was owing to neglecting the contribution of short-range ordering in the sublattice model. The ordered–disordered transition temperatures for both PtRh and $PtRh_3$ are similar to those reported in the literature. The liquid phase remained an ideal solution model and was comparable to that reported in the literature.

Methods

Thermodynamic database

The thermodynamic database was created using the CALPHAD methodology. The core concept of CALPHAD is the systematic parameterization of the Gibbs free energy of all the phases present in the system. The molar Gibbs free energy of each stoichiometric phase in the system was parameterized according to the following polynomial:

$$G_m^{\varphi} = a + bT + cT\ln T + dT^2 + eT^3 + fT^{-1} + \ldots \quad (1)$$

where *a*, *b*, *c*, *d*, *e*, *i*, and *f* are coefficients that must be evaluated from the experimental and calculation results. Polynomial terms can be expanded or omitted to improve the fit based on evaluated data points. The polynomial is generally applied throughout the CALPHAD description not limited to the Gibbs free energy but also for the interaction parameter presented in the system. From molar Gibbs free energy such as entropy (*S*), enthalpy (*H*) and heat capacity (C_p) can be systematically derived:

$$S = -\frac{dG}{dT} = -b - c(1 + \ln T) - 2dT - 3eT^2 + fT^{-2} + \ldots \quad (2)$$

$$H = G + TS = a - cT - dT^2 - 2eT^3 + 2fT^{-1} + \ldots \quad (3)$$

$$C_p = \frac{dH}{dT} = -c - 2dT - 6eT^2 - 2fT^{-2} + \ldots \quad (4)$$

The molar Gibbs free energy for solid-solution phase can be described as follows:

$$G_m^{\varphi} = {}^0G_m^{\varphi} + {}^{ideal}G_{mix}^{\varphi} + {}^{ex}G_{mix}^{\varphi} \quad (5)$$

The molar Gibbs free energy of φ, the solid solution phase (G_m^{φ}), is partitioned into different contributions. ${}^0G_m^{\varphi}$ represents a linear combination of the Gibbs free energies of the end-members. Pt-Rh binary system, ${}^0G_m^{\varphi}$ can be written as:

$${}^0G_m^{\varphi} = x_{Pt}^0 G_{Pt}^{\varphi} + x_{Rh}^0 G_{Rh}^{\varphi} \quad (6)$$

where x_{Pt} and x_{Rh} denotes the mole fraction of the Pt and Rh in the φ phase, respectively. ${}^0G_{Pt}^{\varphi}$ and ${}^0G_{Rh}^{\varphi}$ are the Gibbs free energy of the end-member, which in this case are the Gibbs free energy of pure Pt and Rh in φ phase, respectively. ${}^{ideal}G_{mix}^{\varphi}$ is the ideal mixing energy obtained from the random distribution of atoms in each phase according to the Bragg–William approximation[34]. The ideal mixing energy was calculated using the following formula:

$${}^{ideal}G_{mix}^{\varphi} = RT\left(x_{Pt}\ln x_{Pt} + x_{Rh}\ln x_{Rh}\right) \quad (7)$$

Using only two terms in Equation (5), which represent the molar Gibbs free energy, is called the ideal solution model. ${}^{ex}G_{mix}^{\varphi}$ is the excess energy and represents the deviation from the ideal solution model. The Redlich–Kister polynomial[35] is typically used to represent the excess terms.

$${}^{ex}G_{mix}^{\varphi} = x_{Pt}x_{Rh}\sum_{n=0}^{N} {}^nL_{Pt,Rh}^{\varphi}\left(x_{Pt} - x_{Rh}\right)^n \quad (8)$$

where ${}^nL_{Pt,Rh}^{\varphi}$ is the n^{th}-ordered binary interaction parameter between *Pt* and *Rh* in φ phase, which are typically evaluated using first principles and/or experimental data[36]. The excess term corresponds to the deviation from the ideal mixing. If the reference state is the same phase as φ, excess term is directly corresponding to the enthalpy of mixing in φ phase at 0 K. For the multi-sublattice phase, the ideal mixing energy (${}^{ideal}G_{mix}^{\varphi}$) and the excess energy (${}^{ex}G_{mix}^{\varphi}$) are slightly modified to accommodate the mixing in different

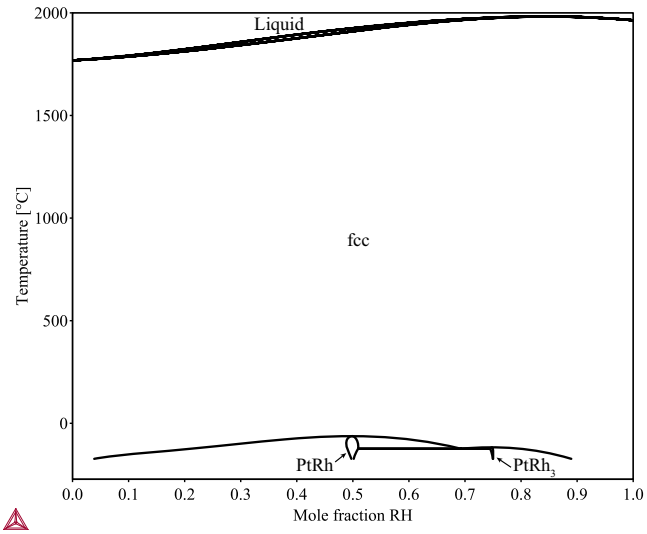


Fig. 9 | Calculated phase diagram of the Pt-Rh binary system based on the thermodynamic database developed using DFT data.

Table 7 | Calculated temperatures and compositions of the invariant reactions in the Pt-Rh binary system obtained from MLIP

Reactions	Temperature, °C	Compositions, mole fraction of Rh		
		x_1	x_2	x_3
fcc ↔ Pt_3Rh + PtRh	−127.58	2.576×10^{-1}	2.506×10^{-1}	4.935×10^{-1}
fcc ↔ PtRh + $PtRh_3$	−62.17 (−124.01)	$6.533(6.929) \times 10^{-1}$	$5.144(5.094) \times 10^{-1}$	$7.419(7.449) \times 10^{-1}$
fcc ↔ Pt_3Rh	−127.46	2.505×10^{-1}	2.505×10^{-1}	N/A
fcc ↔ PtRh	−15.32 (−62.57)	$5.018(4.981) \times 10^{-1}$	$5.018(4.981) \times 10^{-1}$	N/A
fcc ↔ $PtRh_3$	−38.43 (−117.12)	$7.480(7.479) \times 10^{-1}$	$7.480(7.479) \times 10^{-1}$	N/A

The values in parentheses are from DFT calculations.

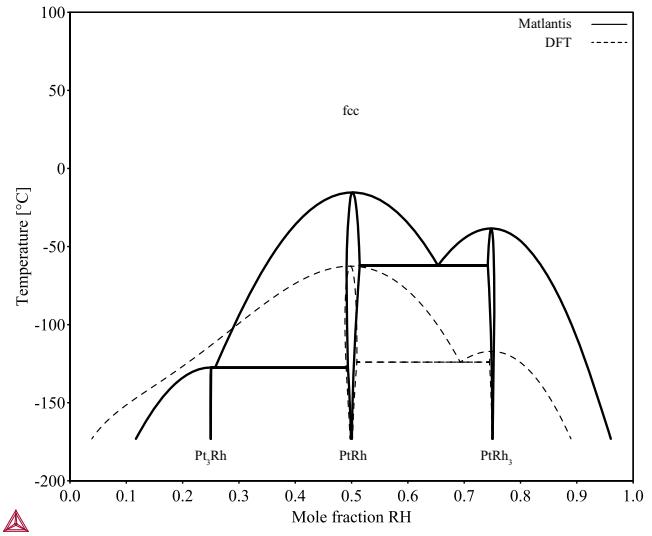


Fig. 10 | Comparison of the calculated Pt-Rh binary phase diagrams from −200 °C to 100 °C obtained using MLIP and DFT. Solid and dashed lines represent the MLIP and DFT results, respectively.

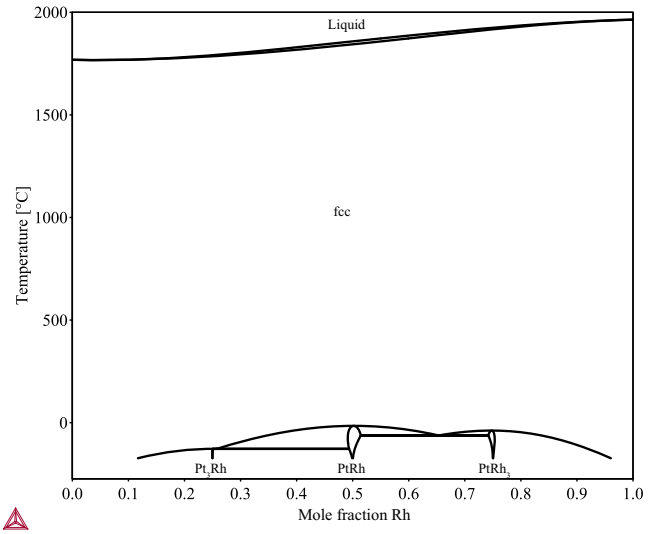


Fig. 11 | Calculated phase diagram of the Pt-Rh binary system based on the thermodynamic database developed using MLIP data.

sublattices[37]. The ideal mixing energy can be expressed as follow:

$$^{ideal}G^{\varphi}_{mix} = iRT\left(y^{I}_{Pt}\ln y^{I}_{Pt} + y^{I}_{Rh}\ln y^{I}_{Rh}\right) + jRT\left(y^{II}_{Pt}\ln y^{II}_{Pt} + y^{II}_{Rh}\ln y^{II}_{Rh}\right) \quad (9)$$

where y^{I}_{x} and y^{II}_{x} are the site fraction of x element in the 1st and 2nd sublattice, respectively. The i and j are the constituent on 1st and 2nd sublattice, respectively. The excess energy term is expanded to the following:

$$\begin{aligned} ^{ex}G^{\varphi}_{mix} = {} & y^{I}_{Pt}y^{I}_{Rh}\left(y^{II}_{Pt}\,{}^{0}L_{Pt,Rh:Pt} + y^{II}_{Rh}\,{}^{0}L_{Pt,Rh:Rh}\right) \\ & + y^{II}_{Pt}y^{II}_{Rh}\left(y^{I}_{Pt}\,{}^{0}L_{Pt:Pt,Rh} + y^{I}_{Rh}\,{}^{0}L_{Rh:Pt,Rh}\right) \end{aligned} \quad (10)$$

where ${}^{n}L_{Pt:Pt,Rh}$ is the nth-order interaction parameter which has the mixing between Pt and Rh elements in the 2nd sublattice. The ":" represent the separation between sublattices in each phase and "," represent the mixing between elements in the sublattice.

Compound energy formalism (CEF)[26] is used for describing the Gibbs free energy of the end-member of the sublattice model. Instead of direct calculation of the Gibbs free energy for each end-member, the Neumann–Kopp rule[38] is used for the approximation for the Gibbs free energy:

$$^{0}G^{A_aB_b}_{m} = x^{0}_{A}G^{A}_{m} + x^{0}_{B}G^{B}_{m} + \Delta_F H - T\Delta_F S \quad (11)$$

$$\Delta_F G = \Delta_F H - T\Delta_F S \quad (12)$$

where ${}^{0}G^{A_aB_b}_{m}$ is the molar Gibbs free energy of the A_aB_b structure, and ${}^{0}G^{A}_{m}$ and ${}^{0}G^{B}_{m}$ are the molar Gibbs free energies of pure A and B, respectively. $\Delta_F G$, $\Delta_F H$, and $\Delta_F S$ are the Gibbs free energy, enthalpy, and entropy of formation, respectively. The entropy of formation was calculated from the negative slope of the Gibbs free energy of the formation plot for each structure with respect to the standard element reference energy.

For a thermodynamic assessment of the interaction parameters, phase diagram, and related thermodynamic properties, the Thermo-Calc Software[39] was used.

Thermodynamic properties

In solid-state physics, the Helmholtz free energy can be partitioned as a function of volume and temperature of a single structure ($F(V, T)$) into the following contributions:

$$F(V,T) = E_{0K}(V) + F_{vib}(V,T) + \ldots \quad (13)$$

where $E_{0K}(V)$ and $F_{vib}(V, T)$ are the ground-state energy and lattice vibrational contributions, respectively. Additional contribution terms, such as thermal electron excitation and spin-ordering magnetic contributions, can also be incorporated. Typically, the CALPHAD-type thermodynamic assessment is preferred using the Gibbs free energy. Using the Legendre transformation, the Gibbs free energy can be expressed as

$$G(P,T) = F(V,T) - \left(\frac{\partial F}{\partial V}\right)_T V \quad (14)$$

The lattice vibrational contribution is calculated from the following equation[40]:

$$F_{vib}(V,T) = k_B T\int_0^{\infty}\ln\left[2\sinh\frac{\hbar\omega}{2k_BT}\right]g(\omega)d\omega \quad (15)$$

where $\hbar$, ω, and $g(\omega)$ are the reduced Planck constant, phonon frequency, and phonon density of states (PDOS), respectively. The PDOS was obtained by solving the dynamic matrix of the force constants[41]. The enthalpy of formation of each endmember was calculated using the following formula:

$$\Delta_F H = E_0^{A_aB_b} - \sum_i x_i E_0^i \quad (16)$$

where $E_0^{A_aB_b}$ is the 0 K energy of the A_aB_b end-member with a and b atoms, x_i is the mole fraction of element i, and E_0^i is the 0 K energy of the i element in its stable structure at room temperature. The crystal structures of the reference energy (E^i) are selected following the same criteria using in the CALPHAD methodology, which is called Standard Element Reference (SER)[42]. If the reference structures are the same as the end-member (A_aB_b), it can be called enthalpy of mixing. The mixing Gibbs free energy is also derived from the similar manner. The binary interaction parameters from Eq. (8) are evaluated from the calculated mixing energy.

The energy and associated thermodynamic properties are calculated using the Matlantis platform[43] which is based on a machine learning interatomic potential (MLIP) that is trained on reference data obtained from quantum-mechanical calculations such as DFT for energies, forces,

and stresses when necessary. It allows the prediction of energies and forces at substantially reduced computational cost while maintaining near-DFT accuracy. The MLIP used in Matlantis is called PreFerred Potential (PFP), which is a neural network potential (NNP) designed as a "universal" MLIP applicable to multi-element, multi-system materials. PFP is based on the message passing neural network (MPNN) and trained on a dataset that covering broad combinations across 96 elements and including diverse structure types (molecules, crystals, slabs, clusters, disordered structures, adsorption structures, etc.)[44]. Its performance is validated via energy/force benchmarks on an out-of-training test set and property-level evaluations including liquid densities (25 organic compounds) and phase-stability metrics based on energy above hull, demonstrating broad applicability across material classes[44]. The DFT calculations were performed using the Vienna Ab initio Simulation Package (VASP)[45] on the generalized gradient approximation (GGA) and the Perdew–Burke–Ernzerhof (PBE)[46] exchange-correlation functional. The DFT results are used for comparing with the data calculated from MLIP. The PAW potential sets comprised of a $5s^1 5d^9$ configuration of valence electrons for Pt and $4s^1 4d^8$ for Rh. All calculations were performed with a spin-polarized enabler and all atomic positions were fully relaxed. Radial distribution function is performed on the relaxed structures to ensure that the relaxed structures remain similar to the parent structure. A cutoff energy of 500 eV and the k-point mesh of Γ-centered Monkhorst–Pack[47] was used for the integration of the Brillouin zone during both the structural relaxations and the final static calculations during the total energy calculations to provide the convergence of electronic energies to a least 0.1 meV per formula unit for all calculations. The 1st order Methfessel–Paxton smearing method[48] was used with a 0.2 eV temperature broadening parameter for electronic occupation. To obtain a highly accurate energy and density of states (DOS) during the final static calculation, the Blöchl correction linear tetrahedron method[49] was used.

The energy of a disordered configuration of the solid solution phase can be calculated using the CEM[21] which allow us to explore the ground state of the randomly mixing in a certain lattice by expanding the internal energy of a system at specific k configuration, E^k, as the following equation

$$E^k = \sum_{\alpha} m_\alpha J_\alpha \sigma_\alpha \tag{17}$$

where m_α is the multiplicities for α cluster, J_α is the effective cluster interaction (ECI) for α cluster and σ_α is the correlation function of the α cluster. For a set of ordered structures, the internal energies are calculated using first-principles calculations, and a set of ECIs can be extracted by matrix inversion. Furthermore, these ECIs can be used to estimate the energies of completely disordered of the system as a function of composition from the above expansion. However, a large numbers of ordered structures are needed to obtain an accurate prediction of the energy for cluster expansion method. Thus, a special quasi-random structure (SQS)[50] which is the structure within a certain number of atoms that has the correlation function (σ_α) closely matched the correlation function of random configuration is used. The Monte Carlo-based code (mcsqs) from the Alloy-theoretical automated toolkit (ATAT)[51] was used for SQS generation. The 0 K mixing energies of the fcc, bcc, and hcp lattices were calculated for the SQSs at 12.5, 25, 37.5, 50, 62.5, 75, and 87.5 at% that used for the evaluation of the interaction parameters from Eq. (8). Additional SQSs were generated to represent the mixing energies of the different elements in the sublattices of the solid-solution compounds. Table 3 shows an example of the calculated correlation functions for the (Pt,Rh)Rh SQS. Up to 12th pairs (pair cluster size of 8.7026 Å and below) of (Pt,Rh)Rh SQS pair correlation functions were aligned with the pair correlation functions of the theoretical random configuration, and all 11th three-body clusters (triplet with cluster size of 6.1688 Å and below) were matched. In this study, the calculated correlation functions up to at least the 12th smallest pair- and 11th smallest triplet-cluster matched the theoretical random correlation functions of the same composition. The details of all the generated SQSs are listed in Table 4.

In this work, short-range ordering contribution and state-of-the-art approaches for liquid free energy calculations are not considered owing to the limited computational resources. We briefly discuss the short-range ordering and state-of-the-art liquid calculations in our previously published work[28].

Data availability

The raw data supporting the findings of this study are not publicly available because they form part of an ongoing study but are available from the corresponding author upon reasonable request. The processed data required to reproduce the phase diagram calculations (i.e., the thermodynamic database) are available from the corresponding author upon reasonable request.

Received: 29 September 2025; Accepted: 25 June 2026;
Published online: 09 July 2026

References

1. Ohtani, H. *The CALPHAD Method* (Springer Berlin Heidelberg, 2006).
2. Chen, C., Ye, W., Zuo, Y., Zheng, C. & Ong, S. P. Graph networks as a universal machine learning framework for molecules and crystals. *Chem. Mater.* **31**, 3564–3572 (2019).
3. Chen, C. & Ong, S. P. A universal graph deep learning interatomic potential for the periodic table. *Nat. Comput. Sci.* **2**, 718–728 (2022).
4. Merchant, A. et al. Scaling deep learning for materials discovery. *Nature* **624**, 80–85 (2023).
5. Deng, B. et al. Chgnet as a pretrained universal neural network potential for charge-informed atomistic modelling. *Nat. Mach. Intell.* **5**, 1031–1041 (2023).
6. Massalski, T., Okamoto, H. & Subramanian, P. *Binary Alloy Phase Diagrams, 2nd ed*. (ASM International, 1990).
7. Raub, E. Metals and alloys of the platinum group. *J. Less-Common Met.* **1**, 3–18 (1959).
8. Niessen, A. et al. Model predictions for the enthalpy of formation of transition metal alloys ii. *CALPHAD* **7**, 51–70 (1983).
9. Lu, Z. W., Wei, S.-H. & Zunger, A. Long-range order in binary late-transition-metal alloys. *Phys. Rev. Lett.* **66**, 1753–1756 (1991).
10. Lu, Z. W., Klein, B. M. & Zunger, A. Ordering tendencies in Pd-Pt, Rh-Pt, and Ag-Au alloys. *J. Phase Equilib.* **16**, 36–45 (1995).
11. Jacob, K. T., Priya, S. & Waseda, Y. Thermodynamic properties and phase equilibria for Pt-Rh alloys. *Metall. Mater. Trans. A* **29**, 1545–1550 (1998).
12. Platzgummer, E. et al. Temperature-dependent segregation on $Pt_{25}Rh_{75}$ (111) and (100). *Surf. Sci.* **419**, 236–248 (1999).
13. Steiner, C. et al. Local order in Pt-47 at%Rh measured with x-ray and neutron scattering. *Phys. Rev. B* **71** (2005).
14. Yuge, K., Seko, A., Kuwabara, A., Oba, F. & Tanaka, I. First-principles study of bulk ordering and surface segregation in Pt-Rh binary alloys. *Phys. Rev. B* **74** (2006).
15. Pohl, J. & Albe, K. Phase equilibria and ordering in solid Pt-Rh calculated by means of a refined bond-order simulation mixing model. *Acta Mater.* **57**, 4140–4147 (2009).
16. Welker, P., Wieckhorst, O., Kerscher, T. C. & Müller, S. Predicting the segregation profile of the $Pt_{25}Rh_{75}$ (100) surface from first-principles. *Phys. Condens. Matter* **22**, 384203 (2010).
17. Maisel, S., Kerscher, T. & Müller, S. No miscibility gap in Pt-Rh binary alloys: a first-principles study. *Acta Mater.* **60**, 1093–1098 (2012).
18. Müller, L. Bestimmung der Schmelzpunkte von Platinlegierungen. *Ann. Phys.* **399**, 9–47 (1930).
19. Acken, J. S. Some physical properties of platinum-rhodium alloys. *J. Res. Natl. Bur. Stand.* **12**, 249 (1934).

20. Curtarolo, S., Morgan, D. & Ceder, G. Accuracy of ab initio methods in predicting the crystal structures of metals: a review of 80 binary alloys. *CALPHAD* **29**, 163–211 (2005).
21. Sanchez, J. M. Cluster expansion and the configurational theory of alloys. *Phys. Rev. B* **81**, 224202 (2010).
22. Benigni, P. et al. Calorimetric measurement of the standard enthalpy of formation of ZnSb at 298 K. *CALPHAD* **58**, 204–213 (2017).
23. Davey, T., Tran, N.-D., Saengdeejing, A. & Chen, Y. First-principles-only CALPHAD phase diagram of the solid aluminium-nickel (Al-Ni) system. *CALPHAD* **71**, 102008 (2020).
24. Zhong, Y., Saengdeejing, A., Kecskes, L., Klotz, B. & Liu, Z.-K. Experimental and computational studies of the Cu-Hf binary system. *Acta Mater.* **61**, 660–669 (2013).
25. Sundman, B. et al. The legacy of "the regular solution model for stoichiometric phases and ionic melts". *J. Phase Equilib. Diffus.* **45**, 934–964 (2024).
26. Hillert, M. The compound energy formalism. *J. Alloys Compd.* **320**, 161–176 (2001).
27. Wolff-Goodrich, S., Hanken, B. E., Solomon, J. M. & Asta, M. Special quasirandom structure modeling of fluorite-structured oxide solid solutions with aliovalent cation substitutions. *Model. Simul. Mater. Sci. Eng.* **23**, 055001 (2015).
28. Saengdeejing, A., Sahara, R. & Toda, Y. Al-Ni-Ti thermodynamic database from first-principles calculations. *CALPHAD* **84**, 102658 (2024).
29. He, Z., Chen, Q. & Selleby, M. Third generation CALPHAD for key elements. *J. Phase Equilib. Diffus.* **45**, 1163–1181 (2024).
30. Sundman, B., Fries, S. G. & Oates, W. A thermodynamic assessment of the Au-Cu system. *CALPHAD* **22**, 335–354 (1998).
31. Ansara, I., Dupin, N., Lukas, H. L. & Sundman, B. Thermodynamic assessment of the Al-Ni system. *J. Alloys Compd.* **247**, 20–30 (1997).
32. Dupin, N., Kattner, U. R., Sundman, B., Palumbo, M. & Fries, S. G. Implementation of an effective bond energy formalism in the multicomponent CALPHAD approach. *J. Res. Natl. Inst. Stand. Technol*. **123** (2018).
33. Alvares, E. et al. A thermodynamic approach to modeling multicomponent feti-based alloys for hydrogen storage. *Scripta Materialia* **259**, 116516 (2025).
34. Bragg, W. L. & Williams, E. J. The effect of thermal agitation on atomic arrangement in alloys. *Proc. R. Soc. London, Ser. A* **145**, 699–730 (1934).
35. Redlich, O. & Kister, A. T. Algebraic representation of thermodynamic properties and the classification of solutions. *Ind. Eng. Chem.* **40**, 345–348 (1948).
36. Lukas, H., Fries, S. G. & Sundman, B. *Computational Thermodynamics* (Cambridge University Press, 2007).
37. Saengdeejing, A., Saal, J. E., Manga, V. R. & Liu, Z.-K. Defects in boron carbide: First-principles calculations and calphad modeling. *Acta Maters.* **60**, 7207–7215 (2012).
38. Kubaschewski, O. Metallurgical thermochemistry. *International Series on Material Science and Technology* **24**, 478 (1977).
39. Andersson, J.-O., Helander, T., Höglund, L., Shi, P. & Sundman, B. Thermo-Calc & DICTRA, computational tools for materials science. *CALPHAD* **26**, 273–312 (2002).
40. Shang, S., Wang, Y. & Liu, Z.-K. First-principles calculations of phonon and thermodynamic properties in the boron-alkaline earth metal binary systems: B-Ca, B-Sr, and B-Ba. *Phys. Rev. B* **75**, 1–11 (2007).
41. van de Walle, A. & Ceder, G. The effect of lattice vibrations on substitutional alloy thermodynamics. *Rev. Mod. Phys.* **74**, 11–45 (2002).
42. Dinsdale, A. SGTE data for pure elements. *CALPHAD* **15**, 317 – 425 (1991).
43. Takamoto, S. et al. Towards universal neural network potential for material discovery applicable to arbitrary combination of 45 elements. *Nat. Commun.* **13**, 2991 (2022).
44. Verification of predicted performance of PFP. https://matlantis.com/en/product/validation/.
45. Kresse, G. & Joubert, D. From ultrasoft pseudopotentials to the projector augmented-wave method. *Phys. Rev. B* **59**, 1758 (1999).
46. Perdew, J. P., Burke, K. & Ernzerhof, M. Generalized gradient approximation made simple. *Phys. Rev. Lett.* **77**, 3865–3868 (1996).
47. Monkhorst, H. J. & Pack, J. D. Special points for Brillouin-zone integrations. *Phys. Rev. B* **13**, 5188–5192 (1976).
48. Methfessel, M. & Paxton, A. T. High-precision sampling for Brillouin-zone integration in metals. *Phys. Rev. B* **40**, 3616–3621 (1989).
49. Blóchl, P. E., Jepsen, O. & Andersen, O. K. Improved tetrahedron method for Brillouin-zone integrations. *Phys. Rev. B* **49**, 16223–16233 (1994).
50. Zunger, A., Wei, S.-H., Ferreira, L. G. & Bernard, J. E. Special quasirandom structures. *Phys. Rev. Lett.* **65**, 353–356 (1990).
51. van de Walle, A., Asta, M. & Ceder, G. The alloy theoretic automated toolkit: a user guide. *CALPHAD* **26**, 539–553 (2002).
52. Jain, A. et al. The Materials Project: a materials genome approach to accelerating materials innovation. *APL Materials* **1**, 011002 (2013).
53. Wolverton, C. Crystal structure and stability of complex precipitate phases in Al-Cu-Mg-(Si) and Al-Zn-Mg alloys. *Acta Mater.* **49**, 3129 – 3142 (2001).
54. Jiang, C., Wolverton, C., Sofo, J., Chen, L.-Q. & Liu, Z.-K. First-principles study of binary bcc alloys using special quasirandom structures. *Phys. Rev. B* **69**, 214202 (2004).
55. Shin, D., van de Walle, A., Wang, Y. & Liu, Z.-K. First-principles study of ternary fcc solution phases from special quasirandom structures. *Phys. Rev. B* **76**, 144204 (2007).

Acknowledgements

This work was supported by the Grants-in-Aid for Scientific Research (KAKENHI; Grant Number 24K01149), the Innovative Science and Technology Initiative for Security Project of the Acquisition, Technology & Logistics Agency (ATLA; Grant Number JPJ004596), which supported the DFT calculations, and the MEXT Program: Data Creation and Utilization-Type Material Research and Development Project (Grant Number JPMXP1122715503), which supported the purchase of Matlantis. The authors gratefully acknowledge the Numerical Materials Simulator supercomputing resources provided by the Research Network and Facility Services Division (RNFS) of the National Institute for Materials Science (NIMS), Japan.

Author contributions

A.S. performed DFT calculations, thermodynamic assessment, and wrote the main manuscript. H.K. performed all the MLIP calculations. R.S., Y.K., K.H., and T.C. provided useful discussions, reviewed, and revised the manuscript.

Competing interests

The authors declare no competing interests.

Additional information

Correspondence and requests for materials should be addressed to Arkapol Saengdeejing.

Reprints and permissions information is available at http://www.nature.com/reprints

Publisher's note Springer Nature remains neutral with regard to jurisdictional claims in published maps and institutional affiliations.

Open Access This article is licensed under a Creative Commons Attribution-NonCommercial-NoDerivatives 4.0 International License, which permits any non-commercial use, sharing, distribution and reproduction in any medium or format, as long as you give appropriate credit to the original author(s) and the source, provide a link to the Creative Commons licence, and indicate if you modified the licensed material. You do not have permission under this licence to share adapted material derived from this article or parts of it. The images or other third party material in this article are included in the article's Creative Commons licence, unless indicated otherwise in a credit line to the material. If material is not included in the article's Creative Commons licence and your intended use is not permitted by statutory regulation or exceeds the permitted use, you will need to obtain permission directly from the copyright holder. To view a copy of this licence, visit http://creativecommons.org/licenses/by-nc-nd/4.0/.

© The Author(s) 2026